EXPERIENCES OF GRID GENERATION AND STEADY/UNSTEADY VISCOUS COMPUTATIONS FOR COMPLEX GEOMETRIES

Lars Tysell
Swedish Defence Research Agency. SE-172 90 Stockholm, Sweden

Keywords: *Viscous computations, Grid generation, Complex geometries*

Abstract

In this paper the results for several studies on viscous flow for complex geometries are summarized. The grid generator TRITET has been used for the generation of unstructured/hybrid grids in two and tree dimensions. The finite volume flow solver EDGE has been used for the flow computations.

1 Background

In [10] - [15] the given grid generation algorithms have mainly been demonstrated for some simple test cases. In [16] a summary of these papers are given. In the present paper the use of these algorithms on real complex geometries are shown together with usage of a finite volume flow solver for viscous flow computations.

2 Flow Solver

The flow solver EDGE, described in [1] and [2], has been used for the flow computations. It solves the compressible Reynolds Averaged Navier-Stokes (RANS) equations. The solver is a node-centered edge-based finite volume solver for arbitrary grid elements. The finite volume scheme is applied on the dual grid. The governing equations are integrated explicitly towards steady state with Runge-Kutta time integration. The convergence is accelerated with an agglomeration multigrid technique and implicit residual smoothing. Several turbulence models can be chosen. The EARSM turbulence model [18] is one of them.

## 3 Computations for a Transonic Transport Configuration in a Wind Tunnel

Within the EUROLIFT II program, see [4] and [9], computations have been performed for the KH3Y model in the ETW (European Transonic Wind Tunnel) facility at $M_\infty = 0.176$ and $Re = 15 \cdot 10^6$. This aircraft model is a transonic transport configuration. The model is a half model mounted on the top wall of the wind tunnel, and it consists of a fuselage and a wing with full span slat and flap. The slat and flap are set in a high lift position. The model is mounted at a distance (peniche) from the wall in order to avoid the influence from the wall boundary layer. CFD solutions at free flight show a slight difference compared to wind tunnel experiments. The intention of this work was to establish if this discrepancy is due to the influence from the wind tunnel walls.

The aircraft model was described by a multi-block structured grid for free flight condition. This grid was imported into the structured multi-block grid generator FFANET [10]. The block connectivities were computed and the surface grid on the boundaries without any connectivity were extracted automatically. This surface description was also modified and improved. The wind tunnel walls and the center body behind the aircraft model were also modeled in this tool.

The flow should be computed for three angles of attack. At first the angle of attack was set
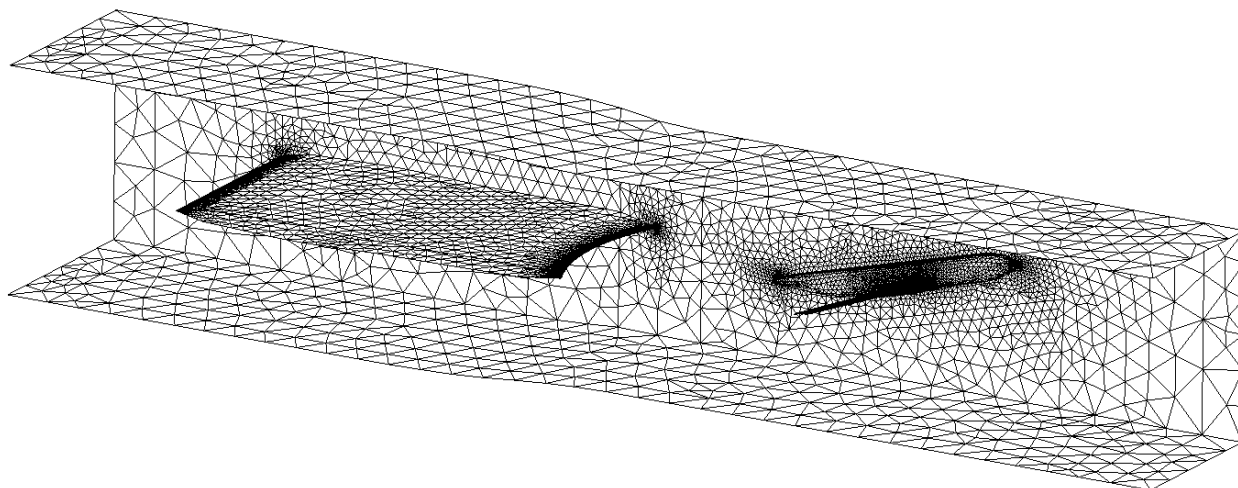
Fig. 1 Coarse surface grid for the KH3Y wind tunnel model.
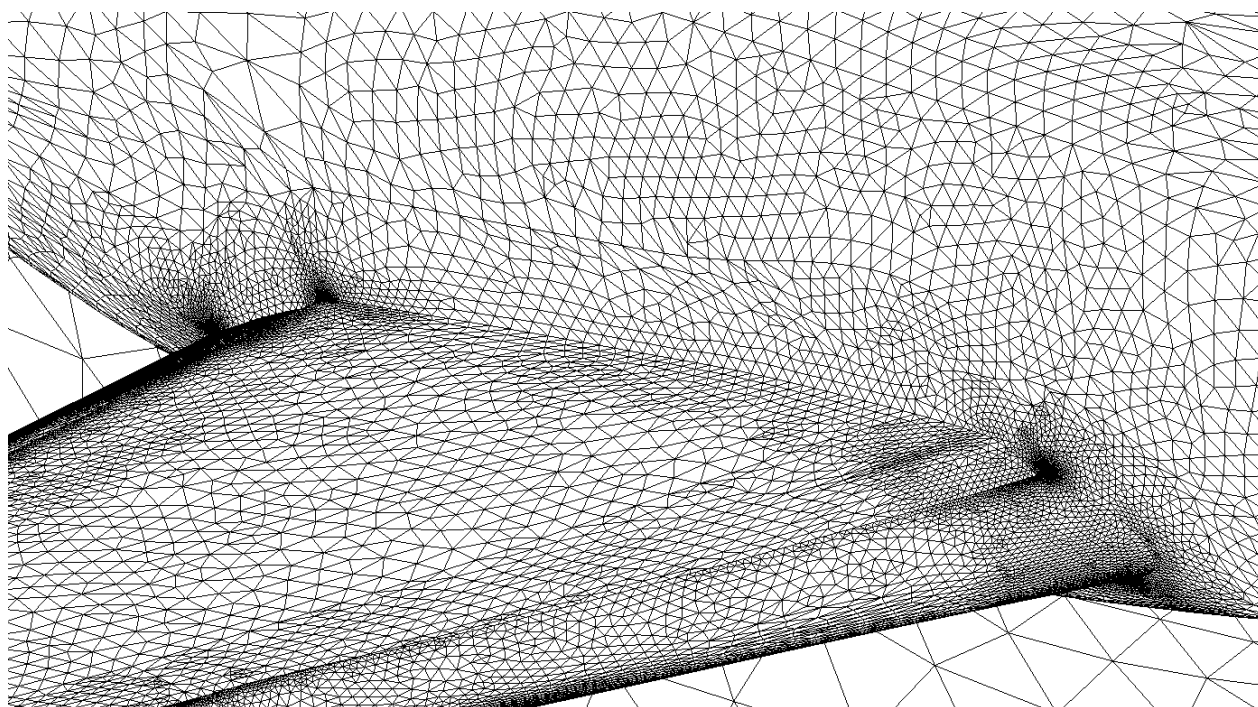
Fig. 2 Wing-Body junction surface grid for the KH3Y model.

to something in the middle of this range. An unstructured grid was generated, see Figure 1, for this angle of attack by first setting the grid resolution, including curvature adaption, by generation of an initial background grid. Then the inviscid flow was computed and a new background grid was generated by adaption. This background grid was used to generate a new unstructured grid with better resolution. The grid point movement functionality in TRITET was then used in order to rotate and deform the grid to give the three angles of attack. The geometry model was also rotated in FFANET to give the geometry definition for these three angles of attack. These three grids were finally used as background grids for the generation of the hybrid grids including the prismatic layers. A close-up of the surface grid at the wing-body junction is shown in Figure 2. An-
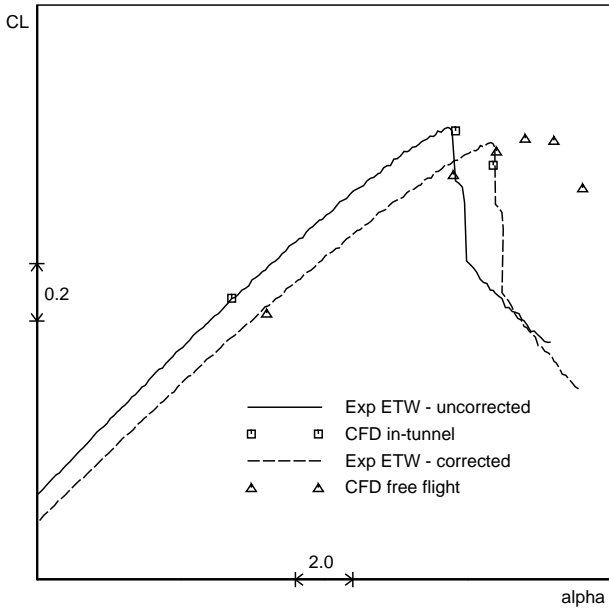
CL

0.2

Exp ETW - uncorrected
□ □ CFD in-tunnel
Exp ETW - corrected
△ △ CFD free flight

2.0

alpha

Fig. 3 C_L vs. α for the KH3Y model.

CL

0.2

Exp ETW - uncorrected
□ □ CFD in-tunnel
Exp ETW - corrected
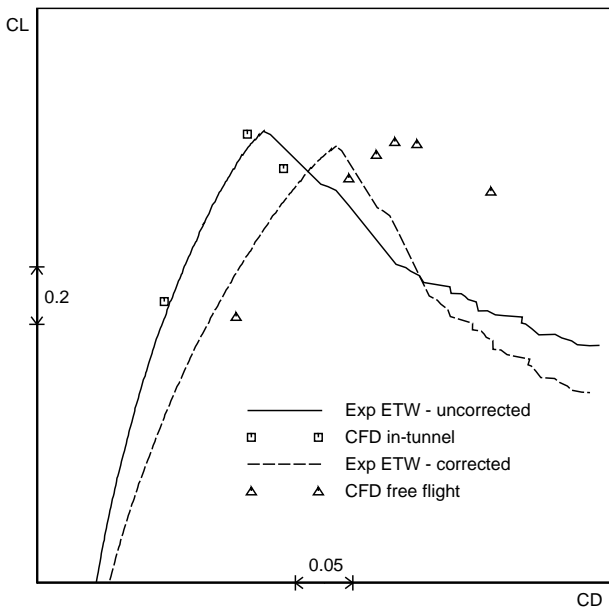△ △ CFD free flight

0.05

CD

Fig. 4 C_L vs. C_D for the KH3Y model.

other way to do this would have been to extract the surface grid for each rotated unstructured grid and use this as input for the hybrid grid generation. The hybrid grids consists of at maximum 30 prismatic layers and approximately $11-12 \cdot 10^6$ nodes. A preliminary viscous computation was done to check that the prismatic grid resolves the boundary layer in order to have the first grid layer

at $y^+ \sim 1.0$.

The final viscous computations for the three angles of attack are reported in [3]. Figure 3 - Figure 4 show the comparison between the computed and the uncorrected experimental forces. As can be seen there is a good agreement, except at the maximum angle of attack, where the computation shows a slightly unsteady behavior, which is not correctly computed by a steady solution. These figures also show the agreement with experiments is better than for the free flight grids, which were also generated within this project. This shows that for proper comparison of high lift computations with experiments it is important also to model the wind tunnel walls.

4 Stretched Grid for a Transonic Transport Configuration

The purpose of this study was to see the effect of grid stretching. In a computation the grid cell sizes have to be small where the gradient in the flow is large and/or the curvature of the geometry is high. At the leading edge of a wing the curvature is high only in one direction. In the span-wise direction the curvature (and flow gradient) is very low. Thus, it would be possible to reduce the number of nodes in the grid by using stretched grid cells in the span-wise direction.
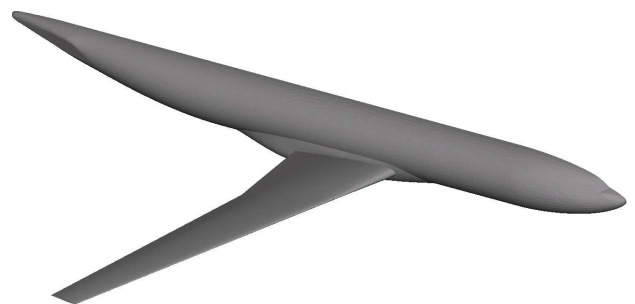

**Fig. 5** Geometry for the wing-body configuration.

The possibility to generate grids adapted to grid curvature has previously been implemented in the grid generator. The configuration used to study the grid effects is the KH3Y clean wing

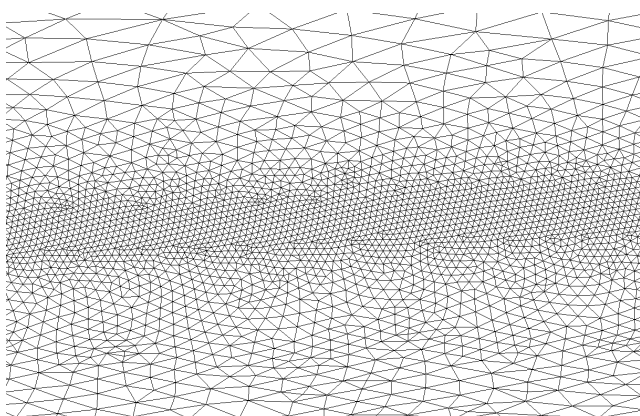| Stretch	No. of nodes	No. of triangles on wing	ΔC_L	ΔC_D
1:1	12272094	520729	-	-
1:5	5235250	176464	0.95 %	1.31 %
1:10	4489861	141166	0.85 %	2.26 %

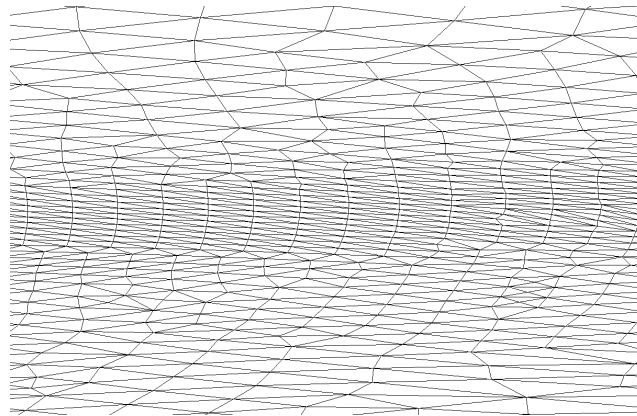**Table 1** C_L and C_D for the wing-body configuration.
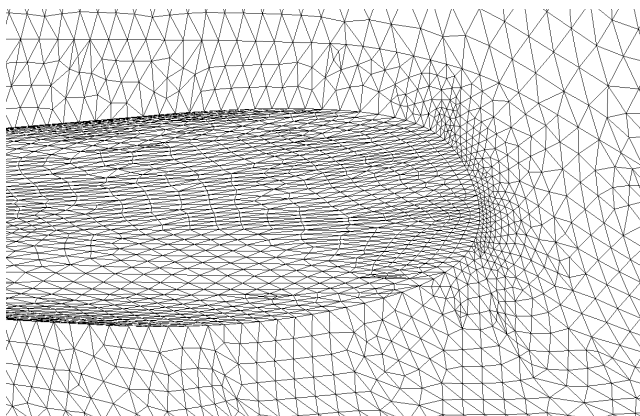
Fig. 6 Grid at wing-body junction for stretch 1:10.
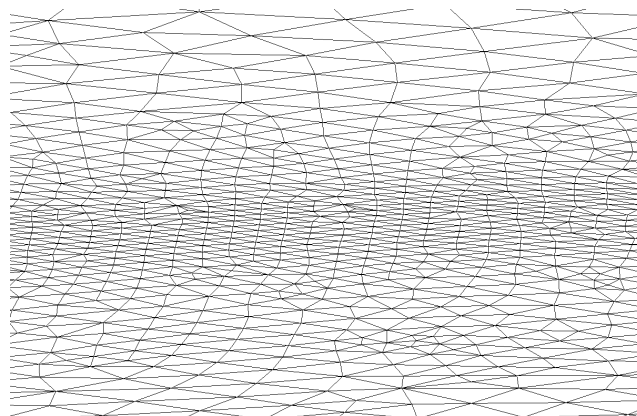
Fig. 8 Grid at wing leading edge for stretch 1:5.

Fig. 7 Grid at wing leading edge for stretch 1:1.

Fig. 9 Grid at wing leading edge for stretch 1:10.

model, without flap and slat, used within the EU-ROLIFT II program, see [4] and [9]. The geometry is shown in Figure 5. The flow condition is $\alpha = 8.0°$ and $Re = 9 \cdot 10^6$ at low speed. The geometry definition was extracted from a structured multiblock grid. Three hybrid grids were generated with stretching 1:1, 1:5 and 1:10. These grids are shown in Figure 6 - Figure 9. All grids have the same resolution in the chord-wise direction. The number of cells in the most stretched grid is only about 36% of the original 1:1 non-stretched grid. As can be seen in Figure 9 the

maximum angle is about 90° (not 180°) for most triangles, since special care has been taken in the Advancing Front algorithm to achieve this. As can be seen in Table 1 the stretching effects the result where little.

5 Steady/Unsteady Computations for a Rear-Fuselage and Empennage Configuration

In this work, performed within the REMFI program, see [8], the flow at high speed for a con-
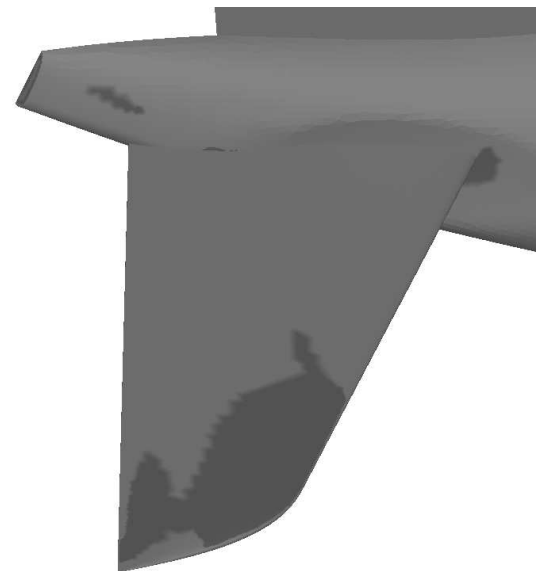
Fig. 10 Surface flow pattern for sealed gap. Steady computation, $Re = 38 \cdot 10^6$, $\alpha = \alpha_2$. In the gap region the velocity vectors are not visible due to high node density.


Fig. 11 Surface flow pattern for sealed gap. Unsteady computation, $Re = 38 \cdot 10^6$, $\alpha = \alpha_2$.

Fig. 12 Surface flow pattern for unsealed gap. Steady computation, $Re = 38 \cdot 10^6$, $\alpha = \alpha_2$.

Fig. 13 Surface flow pattern for unsealed gap. Steady computation, $Re = 38 \cdot 10^6$, $\alpha = \alpha_2$. Dark colour is flow in negative free stream direction.

figuration with and without a gap between the fuselage and the elevator has been investigated. Navier-Stokes computations with an EARSM (Explicit Algebraic Reynolds Stress Model) $k - \omega$ model, see [18], have been performed. Three different horizontal stabilizer setting, each with and without fuselage-elevator gap were studied. For each configuration the results for two angles of attack, α_1 and α_2, were computed. In this study the possibility to import a surface grid generated by commercial grid generators has been used. This surface grid was then used for generation of the hybrid volume grid. The number of grid nodes were about $4.2 \cdot 10^6$, where
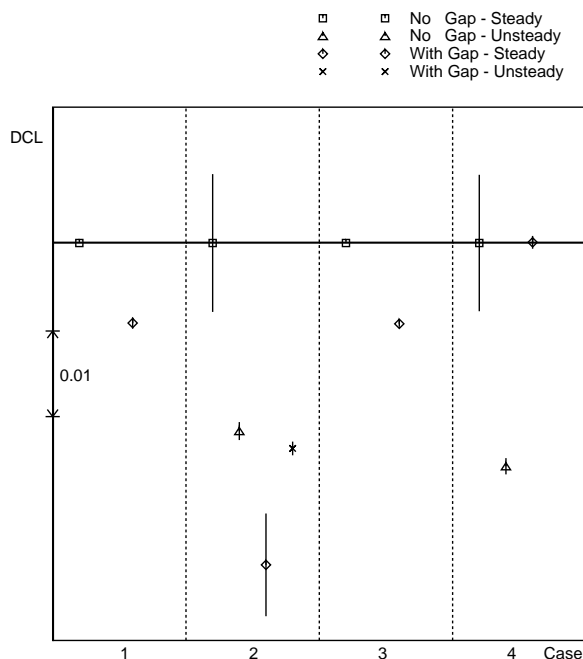
Fig. 14 Difference in C_L between the case with sealed gap and the unsealed gap. Case 1 is $Re = 3 \cdot 10^6$, $\alpha = \alpha_1$. Case 2 is $Re = 3 \cdot 10^6$, $\alpha = \alpha_2$. Case 3 is $Re = 38 \cdot 10^6$, $\alpha = \alpha_1$. Case 4 is $Re = 38 \cdot 10^6$, $\alpha = \alpha_2$.

about $3.3 \cdot 10^6$ nodes are in the prismatic layer. The maximum number of prismatic layers are 25. In Figure 10 - Figure 13 separations can be seen at the wing tip/leading edge of the horizontal stabilizer and at the fuselage behind the elevator. A small separation also can be seen in the fuselage-elevator gap in Figure 13. These separated regions give rise to oscillations in the solution, causing problems to converge the solutions sufficiently for some cases. Thus, for these cases where no steady solution exist unsteady computations have been performed. These unsteady computations show a much better convergence with significantly smaller oscillations than the steady computations. This can be seen in Figure 14 showing the difference in C_L between the configuration with the sealed gap and the unsealed gap. The mean C_L for the steady computation for the sealed configuration is subtracted for each case. The vertical bars show the oscillations in C_L. The differences between

the steady and the unsteady solution for case 2 is not large, but considering the intention of this study it is significant, since the difference in C_L is up to 0.04. This case also shows that the difference in C_L between the sealed and unsealed gap configuration is very different for the steady solutions compared to the unsteady solutions. Another problem with these computations can be seen by comparing Figure 10 and Figure 12. These configurations are the same, except for the sealed/unsealed fuselage-elevator gap. Despite of this the flow pattern at the wing tip/leading edge differs. The grids for these two different configuration have similar, but not coincident, grid resolutions. Thus, a probable cause of the difference in flow pattern is this difference between the grids. For these regions of separated flow the solution may be very dependent on the grid resolution. This study shows that unsteady computations must be done, and the grids must be the same (except at the gap) in order of being able to compute the effect of the unsealed fuselage-elevator gap. Otherwise this effect may be shaded by other effects.
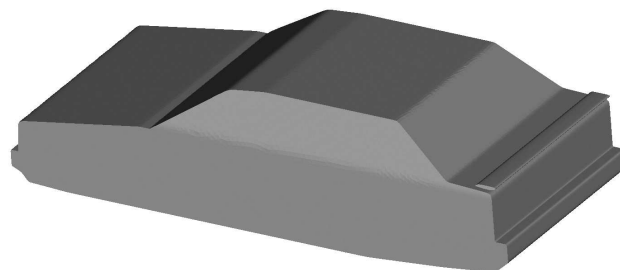

Fig. 15 Geometry for the sedan car configuration.

6 Computation for a Car Configuration

In this work the complex flow at the rear end of a car has been studied. The geometry chosen is the Volvo 850 T5 sedan car, with a rear end wing. Computations have been done both for a two-dimensional geometry and a simplified three-dimensional geometry. The geometry was modeled within FFANET [10]. The geometry is shown in Figure 15, whereas the two-dimensional hybrid grid around the wing at the
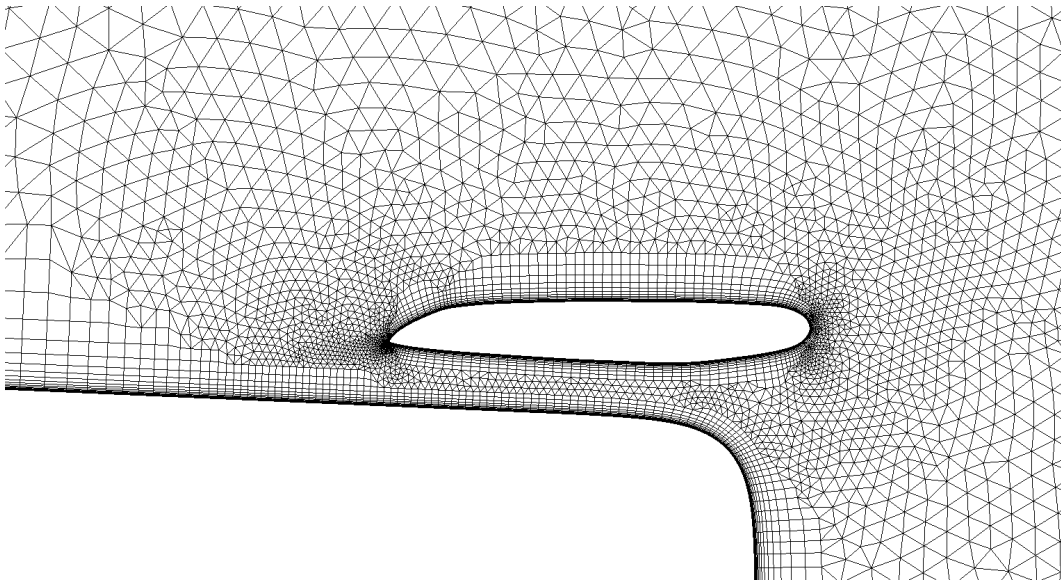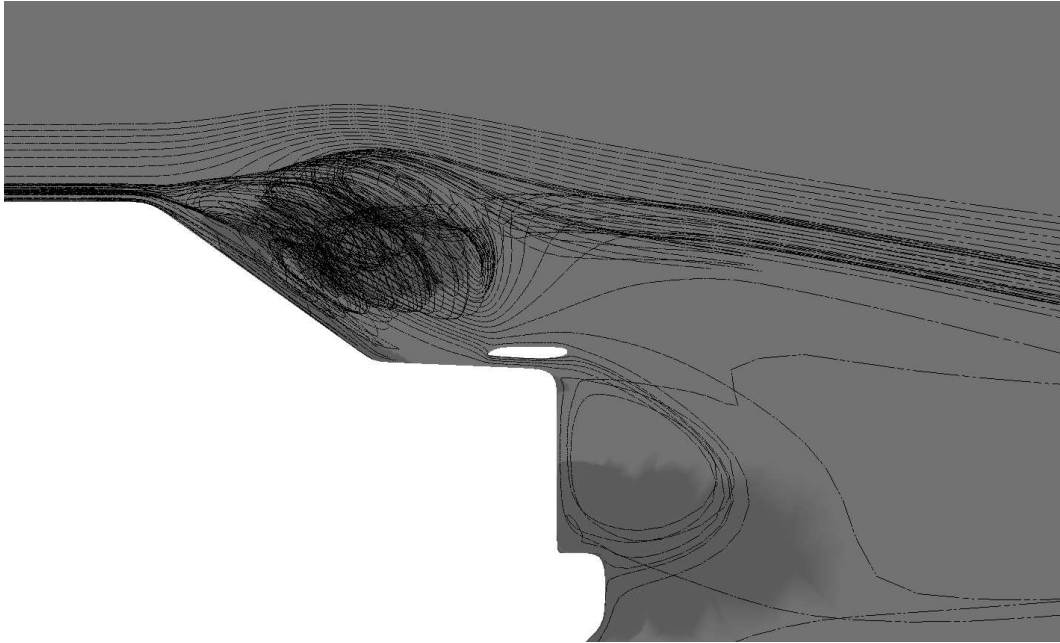
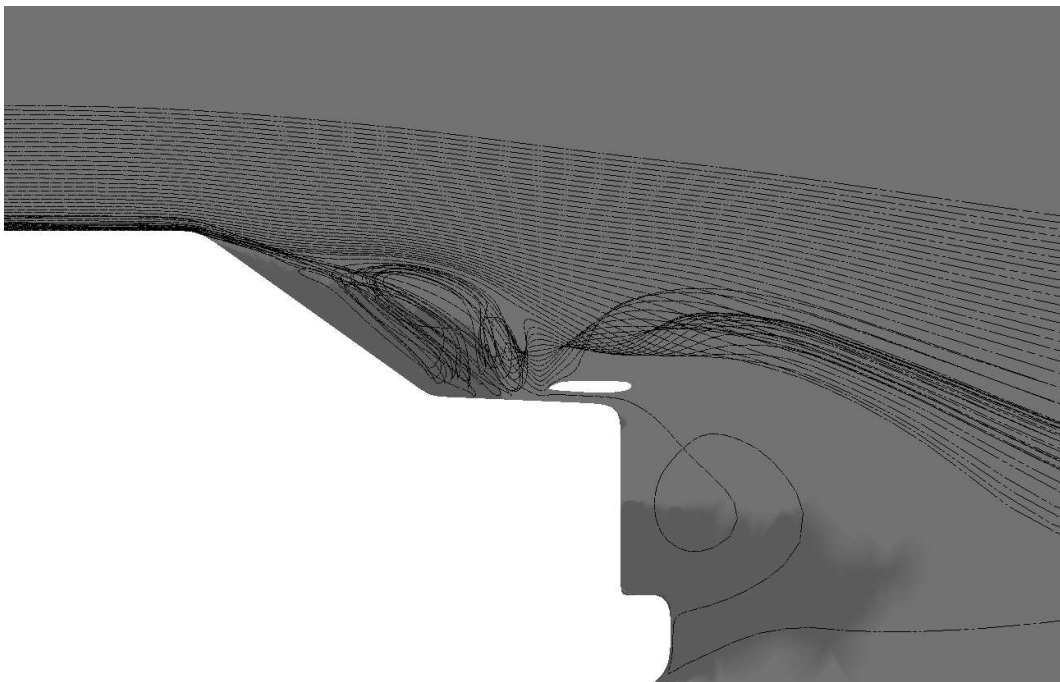**Fig. 16** Two-dimensional grid at the rear end of the car configuration.
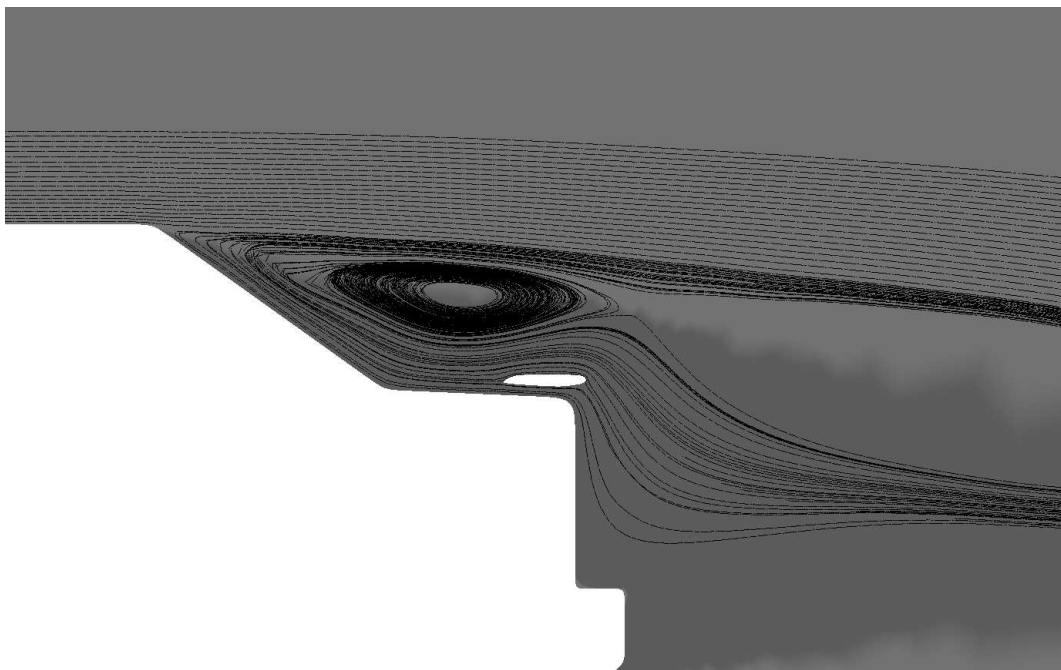
Fig. 17 Steady computation for the two-dimensional car configuration, central scheme.

rear end is shown in Figure 16. The speed was chosen to 240 km/h. Both central and upwind spatial discretization schemes have been used together with the EARSM turbulence model. Study of Figure 17 and Figure 18, which is a cut close to the centre, shows there are big differences in the results between two-dimensional and three-dimensional computations. The unsteady solution in Figure 19 is somewhat different compared to the steady solution. Both streamlines and flow directions are shown in the figures. The dark colour is flow in the reversed direction. This means that for the two-dimensional case the flow is in the reverse direction in a very big region behind the car, and even around the wing. This is not a correct solution according to experiments.

Fig. 18 Steady computation for the three-dimensional car configuration, central scheme.

Fig. 19 Unsteady computation for the three-dimensional car configuration, central scheme.

The three-dimensional central scheme computations shows a more realistic solution. The big differences between the two-dimensional and three-dimensional results are probably due to the fact of the absence in the two-dimensional computation of the flow coming from the sides of the car. This shows that just studying a simple two-dimensional geometry instead of a complex three-dimensional geometry may give totally wrong results. Finally the upwind scheme computation in Figure 20 shows a solution with almost no separation at the upper part of the rear
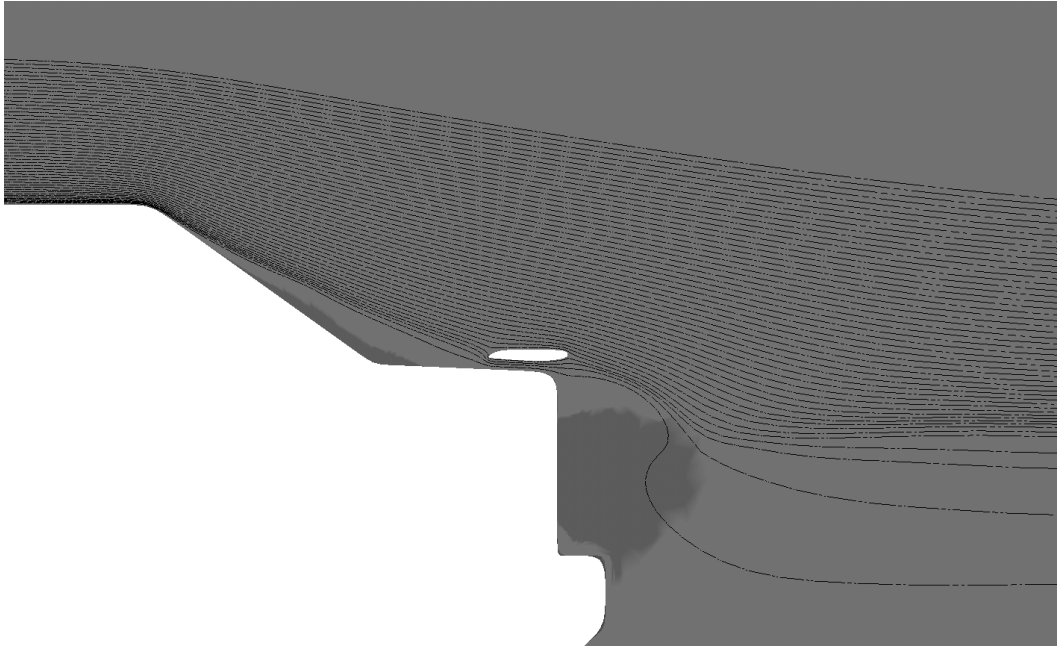
Fig. 20 Steady computation for the three-dimensional car configuration, upwind scheme.

Case	C_L Car	C_L Wing	C_D Total
1	-4.884	$2.28 \cdot 10^{-3}$	0.402
2	-0.498	$-3.60 \cdot 10^{-2}$	0.391
3	-0.495	$-2.93 \cdot 10^{-2}$	0.361
4	-0.838	$-4.43 \cdot 10^{-2}$	0.636

Table 2 C_L and C_D for the car configuration. Case 1: 2D steady, central scheme. Case 2: 3D steady, central scheme. Case 3: 3D unsteady, central scheme. Case 4: 3D steady, upwind scheme. The reference area is the cross section area.

end of the car. This is not a correct solution, which may be caused by too much dissipation. The results are summarized in Table 2 which shows a too high C_D for the 3-dimensional up-wind scheme computation.

7 Transonic Drag Reduction for the Eikon UCAV Configuration

The geometry used within this study is the Eikon configuration designed within the FoT25 project "Design of a Low Signature UCAV" sponsored by the Swedish Defence Material Administration. The Eikon configuration gives slightly too high drag to match the cruise speed requirements

of Mach=0.95. The transonic drag may be reduced by modifying the geometry according to the transonic area rule. According to this theory a body with a cross section area distribution along the center line of the body matching the Sears-Haack area distribution gives the minimum drag. This theory has been shown to work also for bodies being far from slender.
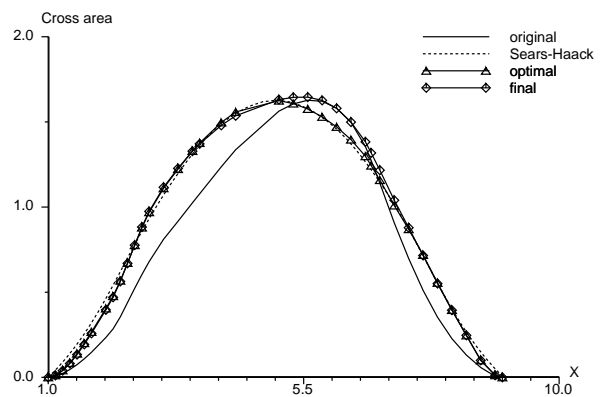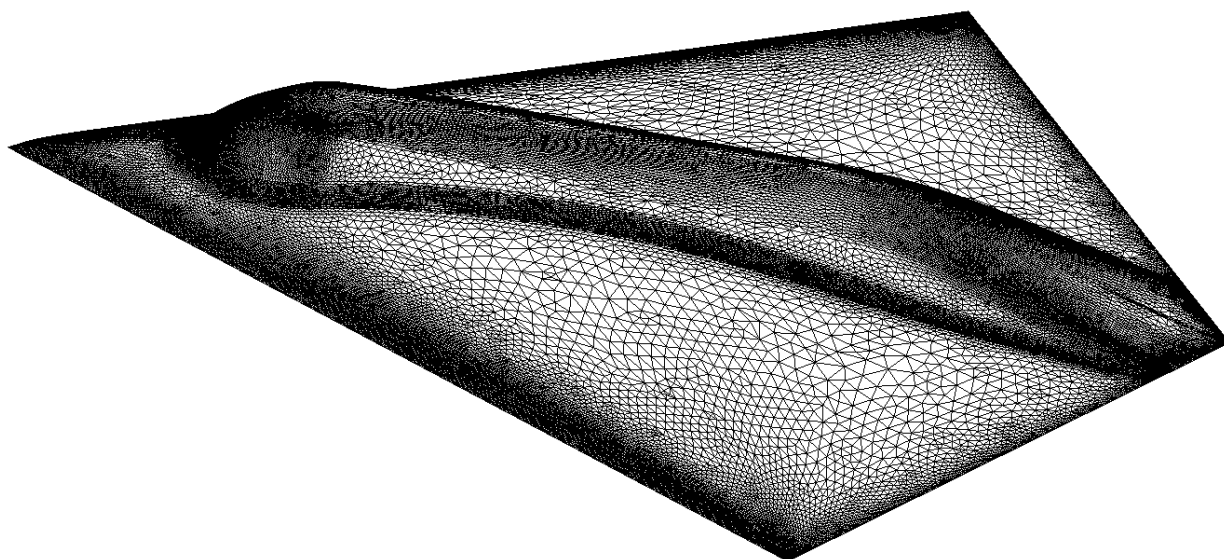

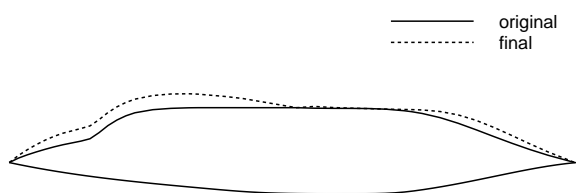**Fig. 21** Cross section area distribution along center axis.

The original Eikon geometry, shown in Figure 22, differs somewhat from this ideal cross section area distribution. It is possible to mod-

Fig. 22 Surface grid for the original configuration.

Fig. 23 Body thickness for optimal geometry.

Fig. 24 Body thickness for final geometry.

ify the geometry to almost match this ideal form. This has been done by making the body and wing thicker (or thinner) along the center line of the body. Only the upper side of the body and wing has been modified. The volume grid for the origi-

nal geometry has been used, by moving the nodes at the surface and in the volume slightly in vertical direction. The nodes not on the surface are moved with the moving grid capability of TRITET, see [14]. Then the grid is very similar to the one used for the original geometry, making sure differences in flow computation results are not caused by different grids. The grid has $2.92 \cdot 10^6$ nodes, where $2.70 \cdot 10^6$ nodes are located in the prismatic layer, consisting of maximum 40 layers. The grid has been adapted at the leading edge of the wing and at the wing-body junction, as can be seen in Figure 22. In Figure 21 the cross section area distribution are showed for the original, Sears-Haack, optimal and final geometry. The optimal geometry is the one as close as possible to the Sears-Haack cross section area distribution. The body thickness for this geometry is slightly reduced at the rear part, compared to the original geometry. Thus the engine may not fit into the body, this can bee seen in Figure 23. In order to fulfill this requirement the geometry was modified so the body is at least as thick as the original body everywhere. This is the final geometry, which is showed in Figure 24. Navier-Stokes finite volume computations have

been done for the original, optimal and final geometry at ground level for Mach=0.95. The angle of attack differs slightly between the three geometries in order to get the same lift, but it is about -1.0 degrees. C_D varies only slightly with C_L around this angle of attack. The computations show the drag is reduced by 8.0% for the optimal geometry, and 6.8% for the final geometry, compared to the original geometry. Despite the body and wing have been made considerably thicker there is a significant reduction in drag.

8 Design of a Variable Wing UAV Configuration

The geometry used within this study is the NUK14 configuration used within the FoT25 project "Adaptive Structures for Aeronautical applications" sponsored by the Swedish Defence Material Administration.

The mission for the UAV configuration in Figure 25 is defined to be divided into two parts. The first part of the mission is flight at Mach 0.8 at 11,000 m, and the second part is flight at Mach 0.8 at very low altitude level. Thus, the wing area used at high altitude is not necessary at low altitude. So an attractive idea is to modify the design to have a wing with variable wing area. It was decided to modify the wing to have a wing span of $0.867 \cdot b$, where b is the original wing span. At high altitude there is an extra wing tip giving a total wing span of $1.133 \cdot b$. The chord of the main wing is $0.496 \cdot b$, whereas the chord of the extra wing tip is $0.238 \cdot b$. At low altitude the design C_L is $0.179 \cdot C_{L_H}$, where C_{L_H} is the C_L at high altitude.

The linear potential flow panel code Wing-Body, see [5] and [6] was used to compute an optimal wing camber distribution giving minimal C_D for a specified C_L for all three configurations. The optimization was done for $C_L = 0.448 \cdot C_{L_H}$, both for the original configuration and the modified configuration without the tip. The modified configuration with tip was also optimized for $C_L = C_{L_H}$, where only the panels on the tip were free to move.

The Wing-Body computations have to be validated by more accurate finite volume Euler and

Fig. 25 Original UAV configuration.

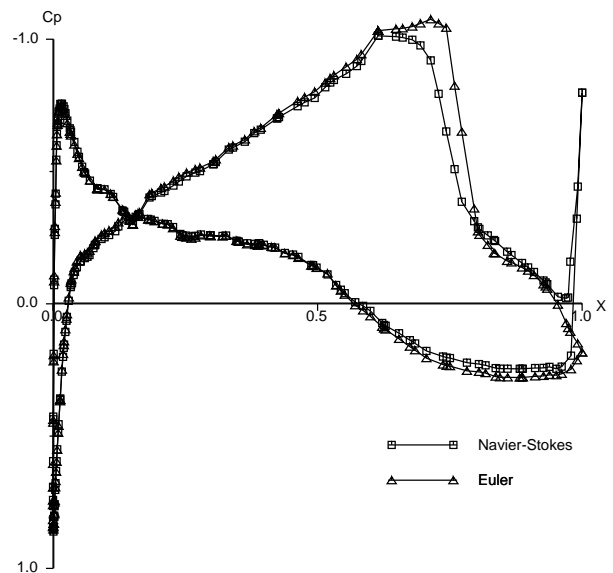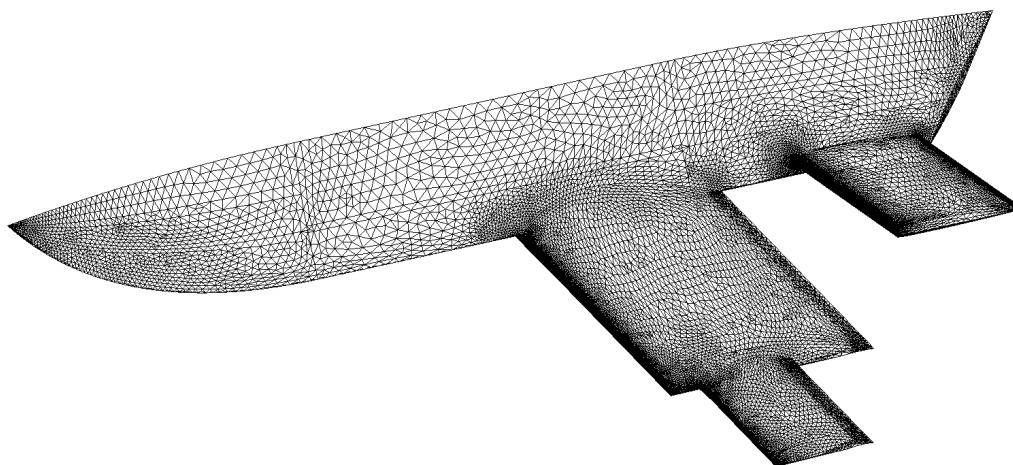**Fig. 26** C_p, range (-1.2,0.2) for low level flight condition.

Fig. 27 C_p for low level flight condition, y=0.458·b.

Navier-Stokes computations. The camber distributions computed by the Wing-Body program was used to modify the original geometry. This CAD-geometry was then imported into the grid

Fig. 28 Surface grid for the modified configuration.

generator by use of the inhouse CAD-interface program SPIDER. The modified configuration with the tip has $0.53 \cdot 10^6$ nodes for the Euler computations and $2.06 \cdot 10^6$ nodes for the Navier-Stokes computations. The surface grid is shown in Figure 28. The same surface grid is used for the Euler and Navier-Stokes computations. The viscous drag from the Navier-Stokes computations have been added to the Euler computations. The improvement in drag for the combined flight condition (half mission at low altitude and half mission at high altitude) is as high as 17.8% for the Euler computations but only around 6.8% for the Navier-Stokes computations. The difference between the Euler and Navier-Stokes computation is difficult to analyze, but may be due to the complex flow at the junction between the short main wing and the body, and the junction between the short main wing and the extra wing tip. There is also a difference in the location of the shock. This shock can be seen in Figure 26 and Figure 27 as well as the non-physical behavior at the trailing edge. In [17] it is shown that the pressure peak at the trailing edge reduces the order of accuracy in the flow solution. The amplitude of this peak is somewhat dependent of the grid structure at the trailing edge. The difference between the inviscid and viscous computations stress the importance of a reliable grid generator being able to generate grids for viscous computations around complex geometries.

References

[1] Eliasson P. Edge - A Navier-Stokes Solver for Unstructured Grids. FOI-R-0298-SE, FOI Swedish Defence Research Agency, 2001.

[2] Eliasson P. Edge, a Navier-Stokes Solver for Unstructured Grids. Proceedings of Finite Volumes for Complex Applications III, ISBN 1-9039-9634-1, pp 527-534, 2002.

[3] Eliasson P. Numerical Validation of a Half Model High Lift Configuration in a Wind Tunnel. AIAA paper AIAA-2007-262, 2007.

[4] EUROLIFT II - European High Lift Programme II, Annex B, A Specified Target Resarch Project of the 6th European Framework Program, contract CRD-2004-502896, 2004.

[5] Gustavsson A. A Computer Program for the Prediction of Aerodynamic Characteristics of Wing-Body-Tail Combinations at Subsonic and Supersonic Speeds. Report FFA AU-635, 1972.

[6] Hedman S. and Tysell L. The FFA Wing Body 81 Computer Program, A Panel Method for determination of Aerodynamic Characteristics at Subsonic and Supersonic Speeds. Technical note FFA AU-1601, 1981.

[7] Lewis R. W., Zheng Y. and Gethin D. T. Three-Dimensional Unstructured Mesh Generation: Part 3. Volume Meshes. *Computer Methods in Applied Mechanics and Engineering* Vol. 134, pp 285-310, 1996.

[8] REMFI - Rear-Fuselage and Empenage Flow Investigation, A Specified Target Resarch Project of

the 6th European Framework Program, contract AST3-CT-2004-502895, 2004.

[9] Rudnik R. and Thiede P. European Research on High Lift Aircraft Configurations in the EURO-LIFT Projects. Proceedings of the , *CEAS/KATnet Conference on Key Aerodynamic Technologies*, Paper 16, pp 1-8, Bremen, Germany, 2005.

[10] Tysell L. and Hedman, S. Towards a General Three-Dimensional Grid Generation System. ICAS Paper ICAS-88-4.7.4, pp 1048-1058, Jerusalem, Israel, 1988.

[11] Tysell L. An Advancing Front Grid Generation System for 3D Unstructured Grids. ICAS Paper ICAS-94-2.5.1, pp 1552-1564, Anaheim, California, USA, 1994.

[12] Tysell L., Berglind T. and Eneroth P. Adaptive Grid Generation for 3D Unstructured Grids. Proceedings of the *6th International Conference on Numerical Grid Generation in Computational Field Simulations*, pp 391-400, International Society of Grid Generation (ISGG), Greenwich, England, 1998.

[13] Tysell L. Hybrid Grid Generation for Complex 3D Geometries. Proceedings of the *7th International Conference on Numerical Grid Generation in Computational Field Simulations*, pp 337-346, International Society of Grid Generation (ISGG), Whistler, British Columbia, Canada, 2000.

[14] Tysell L. Grid Deformation of 3D Hybrid Grids. Proceedings of the *8th International Conference on Numerical Grid Generation in Computational Field Simulations*, pp 265-274, International Society of Grid Generation (ISGG), Honolulu, Hawaii, USA, 2002.

[15] Tysell L. A Higher Order Representation of Unstructured Surface Grids. Proceedings of the *8th International Conference on Numerical Grid Generation in Computational Field Simulations*, International Society of Grid Generation (ISGG), San Jose, California, USA, 2005.

[16] Tysell L. The TRITET Grid Generation System. Proceedings of the *10th ISGG Conference on Numerical Grid Generation*, International Society of Grid Generation (ISGG), Forth, Crete, Greece, 2007.

[17] Tysell L. and Nordström J. Accuracy Evaluation of the Unstructured Node-Centered Finite Volume Method in Aerodynamic Computations. Proceedings of the *10th ISGG Conference on Numerical Grid Generation*, International Society of Grid Generation (ISGG), Forth, Crete, Greece, 2007.

[18] Wallin S. and Johansson A. V. An Explicit Algebraic Reynolds Stress Model of Incompressible and Compressible Flows. *Journal of Fluid Mechanics* Vol. 403, pp 89-132, 2000.

[19] Weatherill N. P., Hassan O., Marcum D. L. and Marchant M. 1994, Grid Generation by the Delaunay Triangulation. VKI Lecture Series 1994-02.

[20] Woodard P., Batina J. and Yang H. Unstructured Mesh Quality Assessment and Upwind Euler Solution Algorithm Validation. *Journal of Aircraft* Vol. 31(3), pp 644-650, 1994.

Copyright Statement